Ultrathin (In, Mg) films on Si(111): A nearly freestanding double-layer metal

Shigemi Terakawa ⬤, Shinichiro Hatta ⬤, Hiroshi Okuyama ⬤, and Tetsuya Aruga ⬤*
Department of Chemistry, Graduate School of Science, Kyoto University, Kyoto 606-8502, Japan

We report on the formation of triple-atomic-layer metal films on Si(111) by deposition of Mg onto In double-layer films. The deposited Mg atoms are intercalated between the In layers and Si substrate and form a buffer layer with $(\sqrt{3} \times \sqrt{3})$ periodicity on an unreconstructed Si(111) surface. Two metal layers with nearly hexagonal close-packed arrangement are stacked in an ABC sequence on the buffer layer. The (In, Mg) triple-layer phase shows free-electron-like electronic structure with circular Fermi surface. Unlike the single Fermi circle of the In double layers, the Fermi surface of the (In, Mg) triple layers is composed of two circles with different radii. The larger and smaller Fermi circles are found to come from bonding and antibonding states between the top and middle layers of the three layers. The bottom layer acts as a buffer layer to saturate the Si dangling bonds and realize a nearly freestanding double-layer metal.

I. INTRODUCTION

Ultrathin metal films on Si surfaces have been of great interest both for fundamental research and technological applications. In general, heavier *p*-block metals form single- or double-atomic-layer metal films with atomically sharp interfaces [1–7], whereas alkali, alkaline-earth, and transition metals react with Si and induce large surface reconstructions and/or even formation of silicides [8–11]. A double-layer phase of In on Si(111) has drawn considerable attention because of its interesting physical properties such as two-dimensional (2D) nearly free-electron band structure with Rashba spin splitting and 2D superconductivity [12–16].

The double-layer phase has a unique quasirectangular array of In atoms with $(\sqrt{7} \times \sqrt{3})$ periodicity on an unreconstructed Si(111) surface. The rectangular structure is interpreted by analogy to the (001) planes of bulk In with a body-centered tetragonal lattice [17,18]. However, the structure contrasts with hexagonal structure of thicker In films and islands grown on buffer layers such as In/Si(111) $(\sqrt{3} \times \sqrt{3})$ [19–25], implying that bonding between In and Si plays a role in stabilizing the rectangular double-layer structure. The interaction between In and Si also affects its electronic structure, which results in deformation from 2D free-electron band structure [12,17,18]. Moreover, the free-electron-like character is strongly suppressed when the thickness is reduced to a single layer [26,27]. As to thicker In films, the layer-dependent band structure evolution has been investigated in terms of quantum well states [23,24] but determination of buffer layer structure and atomic-level thickness control are still challenging.

In the present paper, we report on the atomic and electronic structure of new metallic phases obtained by deposition of Mg onto the double-layer In/Si(111) $(\sqrt{7} \times \sqrt{3})$ phase. We found that the deposited Mg atoms are intercalated between

the In layers and Si substrate and form a crystalline buffer layer with $(\sqrt{3} \times \sqrt{3})$ periodicity, whereas Mg atoms form Mg silicides when deposited directly on the Si(111) (7×7) surface [10,28]. The $(\sqrt{3} \times \sqrt{3})$ phase has a structure consisting of three nearly hexagonal close-packed layers. It shows free-electron-like electronic structure with two circular Fermi contours. The analysis of the character of the metallic bands reveals that the two Fermi circles are attributed to bonding and antibonding states between the top and middle layers and that the bottom buffer layer electronically decouples the metal films from the dangling-bond states of the Si substrate.

II. EXPERIMENTAL AND COMPUTATIONAL METHODS

Experiments were performed in two ultrahigh vacuum chambers with base pressure of $\sim 1 \times 10^{-10}$ Torr. Si(111) substrates (*n*-type) were outgassed at ~ 800 K for hours and cleaned by annealing up to 1500 K. This procedure yielded a well-ordered (7×7) reconstructed surface, which was confirmed by low-energy electron diffraction (LEED) and scanning tunneling microcopy (STM). Angle-resolved photoelectron spectroscopy (ARPES) experiments were done with a hemispherical electron energy analyzer (Scienta R3000) with He I$_\alpha$ radiation ($h\nu = 21.2$ eV) at 30 K. STM measurements (Unisoku USM-1200) were carried out at 78 K with a PtIr tip in the constant-current mode. In and Mg were evaporated from heated crucibles made of alumina and tantalum, respectively. The deposition rate of In was calibrated according to the formation of the In/Si(111) (4×1) phase (1.0 ML) [29], and that of Mg was measured by a quartz microbalance, where 1 ML is defined as the atom density of an unreconstructed Si(111) surface. The In/Si(111) $(\sqrt{7} \times \sqrt{3})$ surface was prepared by deposition of ~ 3ML In on the Si(111) (7×7) surface at room temperature (RT) and annealing at 650 K for half a minute.

Density functional theory (DFT) calculations were performed using projector-augmented-wave (PAW) [30,31]

125402-1

method implemented in the Vienna *ab initio* simulation package (VASP) [32,33]. The generalized gradient approximation (GGA) of Perdew, Burke, and Ernzerhof (PBE) [34] was employed as the exchange-correlation functional. The kinetic energy cutoff was set to 250 eV. The (In, Mg)/Si(111) $(\sqrt{3} \times \sqrt{3})$ surface was modeled by a periodic slab consisting of three Si bilayers, a (In, Mg) bilayer or trilayer, and a vacuum region of $\sim$15 Å. H atoms were used to saturate the Si dangling bonds at the bottom layer of the slab. The bottommost Si atoms were kept fixed at the bulk positions with an optimized Si lattice constant of 5.468 Å. The remaining atoms were relaxed until the residual force on each atom was smaller than 0.01 eV/Å. The Γ-centered $6 \times 6 \times 1$ Monkhorst-Pack [35] k-point mesh was used to sample the surface Brillouin zones (SBZs) for structure searching. For stable configurations, atom positions were further optimized using increased a k-point mesh of $9 \times 9 \times 1$ and a substrate thickness of six Si bilayers, and the electronic band structure was calculated. The structural optimization and band calculation were performed without spin-orbit coupling, because the largest spin-orbit splitting reported for the metallic bands of the In/Si(111) $(\sqrt{7} \times \sqrt{3})$ phase is 0.035 Å^{-1} [36], which is comparable to the momentum broadening of the bands in our ARPES measurements described later. Similar calculation methods were used in the previous study of the $(\sqrt{7} \times \sqrt{3})$ phase [17].

III. RESULTS AND DISCUSSION

Deposition of Mg onto the In/Si(111) $(\sqrt{7} \times \sqrt{3})$ surface [Fig. 1(a)] at 300 K leads to the formation of three new superstructures. At 0.25-ML Mg coverage, a $(2\sqrt{3} \times 2\sqrt{3})$ pattern shows up [Fig. 1(b)]. Above 0.3 ML, $(\sqrt{3} \times \sqrt{3})$ and (4×4) spots simultaneously appear and become intense with increasing Mg coverage. At 1.0 ML, only the $(\sqrt{3} \times \sqrt{3})$ and (4×4) spots are observed [Fig. 1(c)]. Above 1.5 ML, the $(\sqrt{3} \times \sqrt{3})$ and (4×4) spots become weaker, and additional broad spots appear just outside the $(2/3\ 2/3)$ spot and at the symmetrically equivalent positions [Fig. 1(d), 2.5 ML]. One of the spots is indicated by the arrow in Fig. 1(d). The spots are assigned to bulk Mg(0001) (1×1) rotated by 30° with respect to Si(111). This sequential change of the LEED pattern is not influenced by the deposited In amount during the preparation of the initial $(\sqrt{7} \times \sqrt{3})$ phase, where excess In atoms are condensed into islands of several micrometer in diameter [19].

The substrate temperature during the Mg deposition affects the structural evolution. At lower growth temperatures, the intensity of the (4×4) spots, one of which is circled in Fig. 1(c), is weaker and only the $(\sqrt{3} \times \sqrt{3})$ pattern is observed at 210 K [Fig. 1(e)], while the $(2\sqrt{3} \times 2\sqrt{3})$ pattern does not change. The widths of the Mg(0001) spots at higher Mg coverage are broadened at 210 K [Fig. 1(f)]. After the Mg deposition, no change of the LEED patterns was observed down to 30 K except for monotonic increase of the spot intensity according to the Debye-Waller effect. Note that the (4×4) phase is always found together with the $(\sqrt{3} \times \sqrt{3})$ phase and that the surface covered only with the (4×4) phase is not obtained. We focus on the $(2\sqrt{3} \times 2\sqrt{3})$ and $(\sqrt{3} \times \sqrt{3})$ phases, and hereafter we abbreviate their names as the $2\sqrt{3}$ phase and the $\sqrt{3}$ phase, respectively.
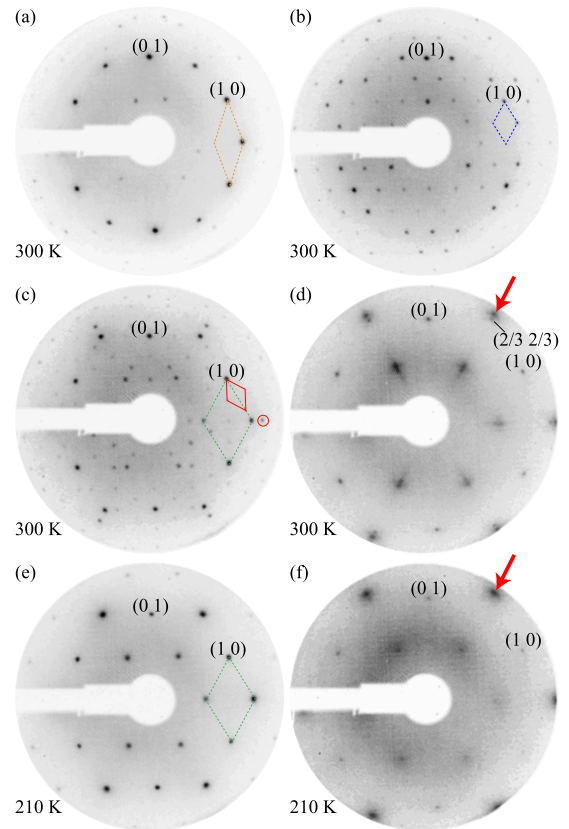

FIG. 1. LEED patterns at 300 K of (a) In/Si(111) $(\sqrt{7} \times \sqrt{3})$, and (In, Mg)/Si(111) (b) $(2\sqrt{3} \times 2\sqrt{3})$, (c) coexisting $(\sqrt{3} \times \sqrt{3})$ and (4×4), and (d) coexisting $(\sqrt{3} \times \sqrt{3})$, (4×4) and Mg(0001). LEED patterns at 210 K of (e) $(\sqrt{3} \times \sqrt{3})$, and (f) coexisting $(\sqrt{3} \times \sqrt{3})$ and Mg(0001). The incident electron energy is [(a), (b), (c), and (e)] 85 and [(d) and (f)] 55 eV. The parallelograms represent the reciprocal unit cells of (a) $(\sqrt{7} \times \sqrt{3})$, (b) $(2\sqrt{3} \times 2\sqrt{3})$, (c) $(\sqrt{3} \times \sqrt{3})$ (dotted) and (4×4) (solid), and (e) $(\sqrt{3} \times \sqrt{3})$. One of the (4×4) spots is indicated by the circle in (c). The arrows in (d) and (f) indicate the Mg(0001) spots.

Figure 2(a) shows a large-scale STM image of the surface with coexisting $2\sqrt{3}$ and $\sqrt{3}$ phases. The darker area on a terrace from the top-right corner is the $2\sqrt{3}$ phase. The close-up view in Fig. 2(b) shows that the structure is rather defective. The characteristic triangular depressions are arranged with $(2\sqrt{3} \times 2\sqrt{3})$ periodicity, but their shapes are irregular. On the other hand, the $\sqrt{3}$ phase looks brighter than the $2\sqrt{3}$ phase on a terrace, and dark lines along the $\langle 11\bar{2} \rangle$ directions are noticeable in Fig. 2(a). Figures 2(c) and 2(d) are high-resolution images of an area including the dark line. On both sides of the line, a well-ordered hexagonal array of bright protrusions is visible. The protrusions belong to the same $(\sqrt{3} \times \sqrt{3})$ grid as displayed in Fig. 2(d). In contrast, dark depressions are present in the opposite half of the cells, indicating that the upper and lower $\sqrt{3}$ phases are antiphase domains. The dark lines are the domain boundaries separating the two domains. Similar domain boundaries are also reported in the (Tl, Mg)/Si(111) $(\sqrt{3} \times \sqrt{3})$ surface [37].

In order to reveal the atomic structure of the $(\sqrt{3} \times \sqrt{3})$ phase, we performed a first-principles total-energy calculation for structures with different In and Mg coverages.
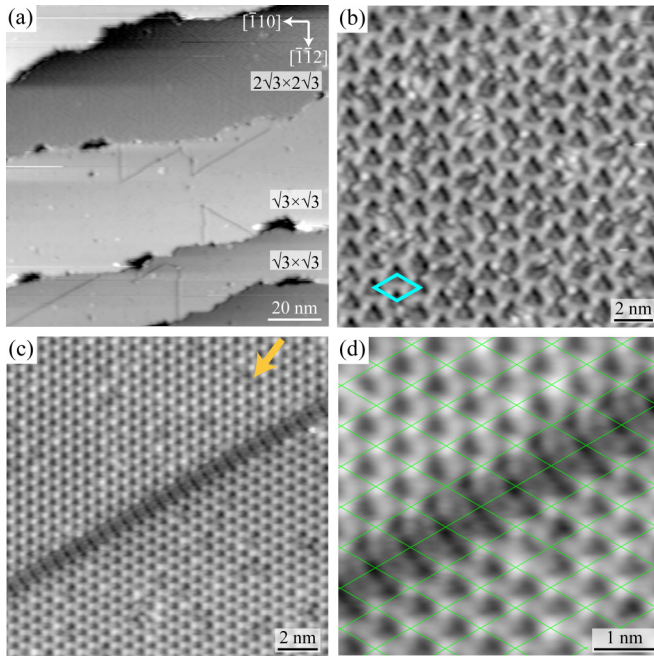
FIG. 2. (a) Large-scale STM image of the surface covered with the (In, Mg)/Si(111) $(2\sqrt{3}\times2\sqrt{3})$ and $(\sqrt{3}\times\sqrt{3})$ phases. High-resolution STM images of (b) the $(2\sqrt{3}\times2\sqrt{3})$ phase and (c) the $(\sqrt{3}\times\sqrt{3})$ phase. The parallelogram in (b) represents the $(2\sqrt{3}\times2\sqrt{3})$ unit cell. (d) Close-up view of the $(\sqrt{3}\times\sqrt{3})$ phase overlaid with the $(\sqrt{3}\times\sqrt{3})$ lattice. The images were obtained at (a) sample bias $V_S= 1.0$ V and tunneling current $I = 0.5$ nA, (b) $V_S = 0.1$ V, $I = 1.0$ nA, and [(c) and (d)] $V_S = 0.5$ V, $I = 1.0$ nA.

We relaxed initial structures and compared their formation energies defined as $E_f = E_{InMg/SiH} - n\mu_{In} - m\mu_{Mg} - 3E_{SiH}$, where $E_{InMg/SiH}$ and E_{SiH} denote total energies of optimized (In, Mg)/Si(111) $(\sqrt{3}\times\sqrt{3})$ and Si(111) (1×1) structures, respectively. μ_{In} and μ_{Mg} are the chemical potentials of In and Mg per atom. n and m are the numbers of In and Mg atoms per $(\sqrt{3}\times\sqrt{3})$ unit cell.

To investigate the relative stability of models with different In and Mg coverages, the chemical potentials μ_{In} and μ_{Mg} have to be specified. As already mentioned, In islands coexist on the pristine In/Si(111) $(\sqrt{7}\times\sqrt{3})$ surface, and the coexistence does not influence the formation of the $\sqrt{3}$ phase. Excess Mg deposition on the $\sqrt{3}$ phase results in the appearance of Mg(0001) spots in LEED, indicating that the extra Mg exists as bulk Mg(0001) films on the $\sqrt{3}$ phase. Therefore we set μ_{In} and μ_{Mg} to the total energies per atom of the respective bulk materials. We also confirmed that the 2D alloys on Si(111) are much more stable than any stable 3D alloys [38].

We first examined all possible configurations of double-layer structures with threefold rotational symmetry whose axis is set at the T_1, T_4 and H_3 sites of Si(111). Structures with each layer composed of four In/Mg atoms per $(\sqrt{3}\times\sqrt{3})$ unit cell were found to show lower E_f values. Then, we tested structures with stacking of two or three layers with four metal atoms per layer per unit cell. The number of In and Mg atoms were respectively set as six to eight and one to six, considering that the initial In coverage of the In/Si(111) $(\sqrt{7}\times\sqrt{3})$ phase is 2.4 ML and that the deposited Mg amount is around 1 ML.
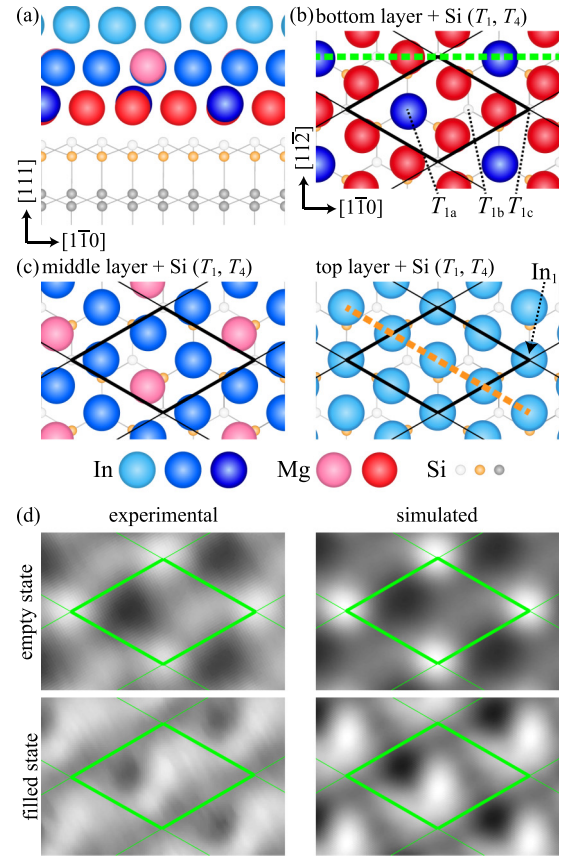

FIG. 3. (a) Side and [(b) and (c)] top views of the optimized structure of the triple-layer model of the (In, Mg)/Si(111) $(\sqrt{3}\times\sqrt{3})$ phase. The top views of the top, middle, and bottom layers are separately presented with Si(T_1) and Si(T_4) atoms for better visualization. (d) (left) Experimental and (right) simulated STM images. The experimental images were obtained at (top) $V_S= 0.5$ V, $I = 1.0$ nA and (bottom) $V_S = -0.4$ V, $I = 2.0$ nA. The solid lines show the $(\sqrt{3}\times\sqrt{3})$ cells. The thick dashed lines in (b) and (c) represent the location of the cross sections shown in Figs. 4 and 9(a), respectively.

It is found that stable structures have a bottom layer configuration of Fig. 3(b) in common. It contains three Mg and an In atoms per $(\sqrt{3}\times\sqrt{3})$ unit cell. In the unit cell, one of the Si dangling bonds at T_{1a} is terminated by the In atom, while the other two at T_{1b} and T_{1c} are saturated by the Mg atoms forming a kagome lattice. We further explored structures by fully relaxing the positions of metal layers relative to the bottom layer of Fig. 3(b).

Figures 3(a)–3(c) illustrate the most stable structure. It consists of three atomic layers of In and Mg, which have nearly close-packed structure stacked in an ABC sequence. The contrasting ABA stacked structure is less stable by 49 meV. The top, middle, and bottom layers respectively have In_4, In_3Mg_1, and In_1Mg_3 compositions per unit cell. Each of the three layers is flat with height difference less than 0.14 Å except for the bottom In atom located 0.25 Å higher than the bottom Mg atoms. The mean interlayer spacing is 2.68 Å (top-middle), 2.49 Å (middle-bottom), and 2.29 Å (bottom-top Si layer). The structure exhibits structural transformation from rectangular arrangement of In atoms in the In/Si(111) $(\sqrt{7}\times\sqrt{3})$ phase to hexagonal arrangement by Mg deposition.
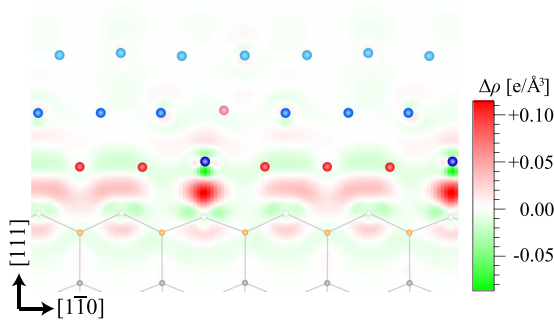
FIG. 4. Charge density difference at the $(11\bar{2})$ plane [the thick dotted line of Fig. 3(b)] of the In_8Mg_4–Si(111) interface. The red and green regions indicate electron accumulation and depletion, respectively.

The average interatomic distance between the top In atoms is 3.33 Å, which agrees with the nearest-neighbor distance of the previously reported hexagonal In films and islands [19,22,24]. The atom density is only 0.5% higher compared to the (101) plane, the closest packed plane, of bulk bct In [39].

Figure 3(d) shows experimental and simulated STM images. The simulated empty-state and filled-state images were generated from the local density of states 0–0.5 eV above and 0–0.4 eV below the theoretical Fermi level [40], respectively. The calculated empty-state image with bright protrusions and dark depressions closely resembles the experimental STM image with a sample bias of 0.5 V. Although all the top In atoms are located at nearly the same height, only the atom on the T_{1c} site, which is labeled In_1 in Fig. 3(c), appears as a bright protrusion. The other top In atoms are not clearly resolved, and the dark depression is seen on the T_{1a} site, where the bottom In atom resides. In the filled-state image, the In_1 atom becomes darker, while the position of the dark depression does not change. The area on the Mg atom of the middle layer becomes brighter. The calculated filled-state image also shows resemblance to the experimental one with a sample bias of −0.4 V. The two domains observed in the STM image [Fig. 2(d)] can be interpreted as structures whose lateral positions of the middle and bottom layers are reversed but those of the top layers are identical.

In order to investigate the bonding character of the interface, the charge density difference $\Delta\rho$ was calculated. $\Delta\rho$ is defined as $\Delta\rho = \rho_{In_8Mg_4/Si(111)} - \rho_{In_8Mg_4} - \rho_{Si(111)}$, where $\rho_{In_8Mg_4/Si(111)}$, $\rho_{In_8Mg_4}$ and $\rho_{Si(111)}$ denote the charge density of the In_8Mg_4/Si(111), In_8Mg_4 and Si(111), respectively. Figure 4 displays the $\Delta\rho$ values in the $(11\bar{2})$ plane. The red and green regions indicate electron accumulation and depletion, respectively. Strong electron accumulation is seen at the metal-silicon interface. First, electron accumulation is strongly localized between the bottom In and top Si(T_{1a}) atoms, which indicates that the Si dangling bond is terminated by a covalent bond with In. Second, electron accumulation is also seen between the bottom Mg and top Si(T_{1b}, T_{1c}) atoms. The accumulated region is delocalized among the bottom Mg atoms and the Si atom, suggesting that the dangling bond is saturated by electrons from the surrounding three Mg atoms [see also Fig. 3(b)]. These bonding characters greatly contribute to the stability of the bottom-layer structure of

Fig. 3(b), and hexagonal layers of top and middle layers stably grow on it. A quite similar bottom-layer structure was reported in the double-layer (Tl, Mg)/Si(111) ($\sqrt{3}\times\sqrt{3}$) phase [37].

The triple-layer model has an In_8Mg_4 composition with a total coverage of 2.67 ML (In) and 1.33 ML (Mg). The In coverage is slightly higher than the initial coverage of 2.4 ML. The coverage deviation is compensated by other structures. Although the In islands on the ($\sqrt{7}\times\sqrt{3}$) surface can be related to the coverage compensation, two 2D structures with the ($\sqrt{3}\times\sqrt{3}$) periodicity are suggested from the experiments and calculation. One is the In_5Mg_3 double-layer ($\sqrt{3}\times\sqrt{3}$) structure suggested from ARPES experiments and band structure calculation as discussed later. The other is the In_7Mg_5 triple-layer structure, which is the second most stable structure in the calculation. The atomic structure is the same as that of the In_8Mg_4 structure [Fig. 3] except that the In_1 atom is replaced by a Mg atom. The formation energy is calculated to be 11 meV higher than that of the In_8Mg_4 model. Given the growth temperature of 210 K ($k_BT = 18$ meV, k_B: the Boltzmann constant), the In_7Mg_5 structure coexists with the In_8Mg_4 structure as point defects, and appears as randomly distributed dark protrusions, one of which is indicated by the arrow in the STM image of Fig. 2(c). The number of the dark protrusions is ∼7% of the total protrusions. It should be noted here that the $2\sqrt{3}$ phase would also have double-layer structure in consideration of the deposited Mg amount of 0.25 ML and the STM appearance darker than the triple-layer $\sqrt{3}$ phase, although we do not know the precise atomic structure.

Figure 5(a) shows ARPES Fermi surface map of the (In, Mg)/Si(111) ($2\sqrt{3}\times2\sqrt{3}$) phase. Circular Fermi contours surrounding the (1×1) SBZs are noticeable. Fine features are also seen in the ($2\sqrt{3}\times2\sqrt{3}$) SBZs. The observed Fermi contours result from overlapping of circles with the same radius centered at the $\bar{\Gamma}$ points of the ($2\sqrt{3}\times2\sqrt{3}$) SBZs as illustrated by the solid curves in the lower-right part of Fig. 5(a). The circular Fermi surface indicates 2D free-electron-like electronic properties of the $2\sqrt{3}$ phase. Similar circular Fermi surface is known for the In/Si(111) ($\sqrt{7}\times\sqrt{3}$) phase [12]. The effect of the Mg deposition is found as a little increment in the radius of the Fermi circle (k_F): $k_{Fx} = k_{Fy} = 1.42$ Å^{-1} for the (In, Mg)/Si(111) ($2\sqrt{3}\times2\sqrt{3}$) phase and $k_{Fx} = 1.40$ Å^{-1}, $k_{Fy} = 1.41$ Å^{-1} for the In/Si(111) ($\sqrt{7}\times\sqrt{3}$) phase. Moreover, the Fermi circle of the $2\sqrt{3}$ phase shows little deviation from a perfect circle, while that of the In/Si(111) ($\sqrt{7}\times\sqrt{3}$) phase exhibits significant difference in butterfly features [see Fig. 7(b)] [12,18].

We present ARPES band maps along the high symmetry lines $\bar{\Gamma}$-$\bar{M}$ and $\bar{\Gamma}$-$\bar{K}$-$\bar{M}$-$\bar{K}$ of the ($2\sqrt{3}\times2\sqrt{3}$) SBZs in Figs. 5(b) and 5(c). The bands dispersing downward from $\bar{\Gamma}_0$ at 0.65–0.95 and 1.8 eV are Si valence bands. The lower band is the Si bulk valence band and it is located at 0.16 eV higher binding energy than that of the In/Si(111) ($\sqrt{7}\times\sqrt{3}$) phase. The upper bands are subbands due to the quantum confinement in the narrow space-charge layer with upward band bending [41]. There are many surface-state bands, and we focus on those crossing the Fermi level E_F and label them S_1–S_5. The S_1 and S_2 bands along $\bar{\Gamma}$-$\bar{M}$ disperse upward from $\bar{M}$ and intersect E_F near $\bar{M}$ and $\bar{\Gamma}$, respectively. Along $\bar{\Gamma}$-$\bar{K}$,
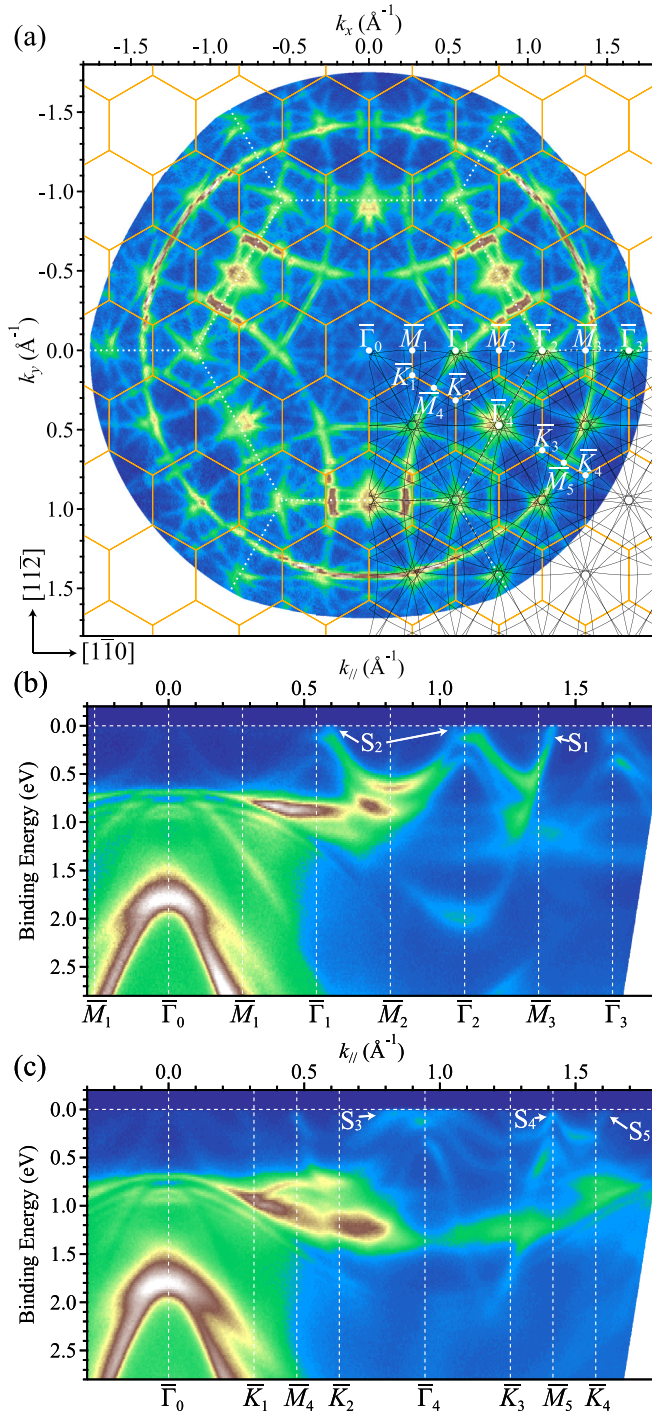
FIG. 5. (a) Fermi surface map of the (In, Mg)/Si(111) $(2\sqrt{3} \times 2\sqrt{3})$ phase. The energy window was 20 meV and the spectra were symmetrized according to the mirror and threefold rotational symmetries of Si(111). The solid and dotted lines are the $(2\sqrt{3} \times 2\sqrt{3})$ and (1×1) SBZs, respectively. The solid circles in the lower-right part display circles with a radius of $k = 1.42$ Å^{-1} centered at $\overline{\Gamma}$ points of the $(2\sqrt{3} \times 2\sqrt{3})$ SBZs. Band maps along (b) $\overline{\Gamma}$-$\overline{M}$ and (c) $\overline{\Gamma}$-$\overline{K}$-$\overline{M}$-$\overline{K}$ of the $(2\sqrt{3} \times 2\sqrt{3})$ SBZs. The (In, Mg)-induced metallic surface states are denoted as S_1–S_5.
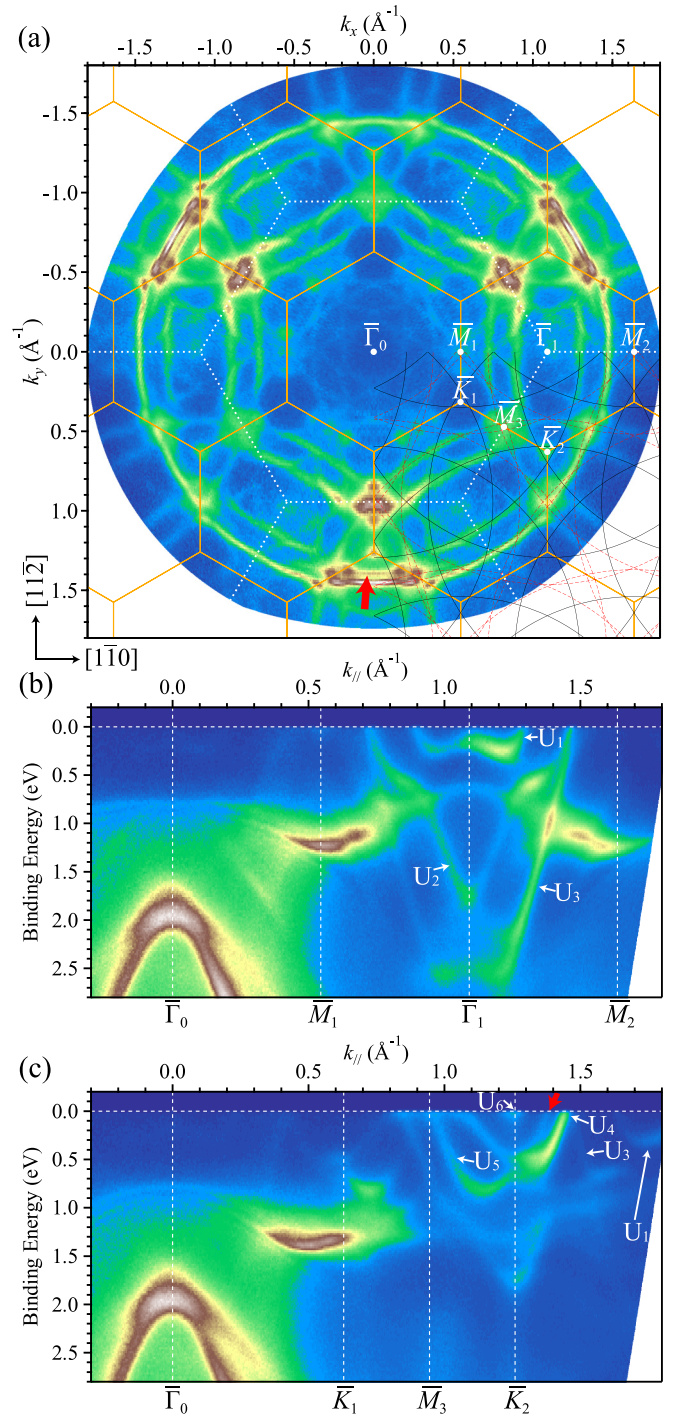
FIG. 6. (a) Fermi surface map of the (In, Mg)/Si(111) $(\sqrt{3} \times \sqrt{3})$ phase. The energy window was 20 meV and the spectra were symmetrized according to the mirror and threefold rotational symmetries of Si(111). The solid and dotted lines are the $(\sqrt{3} \times \sqrt{3})$ and (1×1) SBZs, respectively. The solid and dashed circles in the lower-right part display circles centered at $\overline{\Gamma}$ points of the $(\sqrt{3} \times \sqrt{3})$ SBZs with radii of $k = 1.29$ and 1.46 Å^{-1}, respectively. Band maps along (b) $\overline{\Gamma}$-$\overline{M}$ and (c) $\overline{\Gamma}$-$\overline{K}$-$\overline{M}$-$\overline{K}$ of the $(\sqrt{3} \times \sqrt{3})$ SBZs. The (In, Mg)-induced metallic surface states are denoted as U_1–U_6. The thick arrows in (a) and (c) indicate the bands of the coexisting double-layer $(\sqrt{3} \times \sqrt{3})$ phase.

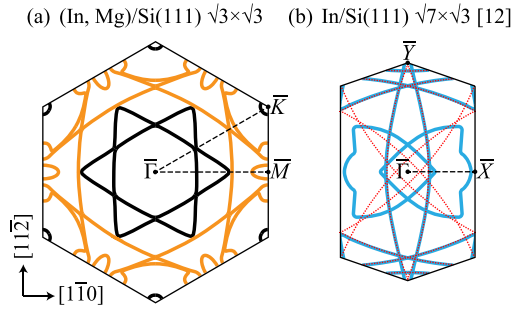(a) (In, Mg)/Si(111) $\sqrt{3}\times\sqrt{3}$ (b) In/Si(111) $\sqrt{7}\times\sqrt{3}$ [12]

FIG. 7. Schematic drawings of the experimental Fermi surface of (a) the (In, Mg)/Si(111) ($\sqrt{3}\times\sqrt{3}$) phase and (b) the In/Si(111) ($\sqrt{7}\times\sqrt{3}$) phase [12]. The black and orange (light gray) curves in (a) represent the contours ascribed to the inner and outer circles, respectively. The dotted curves in (b) describe ellipses centered at $\overline{\Gamma}$ points of the ($\sqrt{7}\times\sqrt{3}$) SBZs with a radius of $k = 1.41$ Å^{-1} along [1$\overline{1}$0] and 1.40 Å^{-1} along [11$\overline{2}$].

the S_3 band dispersing above 0.5 eV touches E_F near $\overline{\Gamma}$. The S_4 band shows a rapid change of slope at 0.05 Å^{-1} from $\overline{M}$ and crosses E_F at $\overline{M}$. In addition, the electron pockets S_5 are present at $\overline{K}$. The steep S_1 and S_4 bands correspond to the Fermi circle centered at $\overline{\Gamma}_0$.

Next we show ARPES data of the (In, Mg)/Si(111) ($\sqrt{3}\times\sqrt{3}$) phase. In the Fermi surface map of Fig. 6(a), circular features are also clearly visible. In contrast to the single k_F value of the $2\sqrt{3}$ phase, the Fermi surface of the $\sqrt{3}$ phase is composed of two concentric circles centered at $\overline{\Gamma}$ points of the ($\sqrt{3}\times\sqrt{3}$) SBZs with distortion from ideal circles in the vicinity of the SBZ boundaries. The solid and dashed circles in the lower-right part of Fig. 6(a) depict circles with $k = 1.29$ and 1.46 Å^{-1}, respectively. We call the smaller one the "inner" circle and the larger one the "outer" circle. The relationship between the observed Fermi contours and the two circles is schematically drawn in Fig. 7(a), where the black curves represent the contours related to the inner circle, and the orange (light gray) curves to the outer circle. The inner circles form a hexagram centered at $\overline{\Gamma}$ and circles at $\overline{K}$. The outer circles form a larger hexagram with the corners going outside the ($\sqrt{3}\times\sqrt{3}$) SBZ, arcs which are surrounding $\overline{K}$ and bent near the zone boundaries, and ellipses at $\overline{M}$.

In Figs. 6(b) and 6(c), we show band maps along $\overline{\Gamma}$-$\overline{M}$ and $\overline{\Gamma}$-$\overline{K}$-$\overline{M}$-$\overline{K}$ of the ($\sqrt{3}\times\sqrt{3}$) SBZs. The Si valence bands move to higher binding energy by 0.16 eV compared with the $2\sqrt{3}$ phase, and thus 0.32 eV compared with the In/Si(111) ($\sqrt{7}\times\sqrt{3}$) phase. At the $\overline{\Gamma}_1$ point, the replica band is seen at $\sim$0.7 eV. This higher energy shift indicates decreasing band bending because the pristine ($\sqrt{7}\times\sqrt{3}$) phase on n-type Si(111) substrates induces an upward band bending larger than 0.5 eV [41]. We measured the values of work function from the cutoff energy of secondary electrons. The formation of the $\sqrt{3}$ phase decreases the work function by 0.25 eV in comparison with the ($\sqrt{7}\times\sqrt{3}$) phase. This work function change has two contributions, as is well known for adsorbate-induced work function change for semiconductor substrates: the band bending and the surface dipole [42,43]. We estimated the band bending change at -0.32 eV from the Si valence band shift at $\overline{\Gamma}_0$. Therefore the dipole contribution

is $+0.07$ eV. The positive value is opposite to that reported for the Si surfaces covered with other electropositive atoms, like alkali metals, where alkali-metal atoms are adsorbed on the top layer of the surface and make a negative dipole contribution [44,45]. The positive dipole contribution observed for the (In, Mg)/Si(111) ($\sqrt{3}\times\sqrt{3}$) phase implies that the more-positive Mg atoms are located beneath the less-positive In atoms, which is consistent with the theoretical model in Fig. 3.

We then describe surface-state bands near E_F. Along $\overline{\Gamma}$-$\overline{M}$ [Fig. 6(b)], three metallic bands labeled U_1, U_2 and U_3 are clearly observed. The U_1 band has a "W" shape with the bottom at $\sim$0.4 eV, and the U_2 band has a "V" shape with the bottom at $\sim$1.7 eV extending toward the $\overline{M}$ points above 0.8 eV. The U_1 and U_2 bands cross E_F at 1.29 and 1.46 Å^{-1}, respectively, on the $\overline{\Gamma}_1$-$\overline{M}_2$ line. The U_3 band exhibits a steep dispersion above 2.6 eV and almost degenerates with the U_2 band near E_F. A blurred feature is also observed at $\overline{M}_1$. The E_F crossings of the U_1–U_3 bands agree with the two Fermi circles shown in Figs. 6(a) and 7(a).

Along $\overline{\Gamma}$-$\overline{K}$-$\overline{M}$-$\overline{K}$ [Fig. 6(c)], the inner Fermi circle has components of the electron pockets U_6 at $\overline{K}$ and the U_1 band, which is only weakly observed in the far right of Fig. 6(c). The outer Fermi circle appears as the U_3 and U_4 bands on the $\overline{\Gamma}$-$\overline{K}$ line, and the U_4 band crosses E_F at 1.44 Å^{-1}. The U_4 band has energy minima of 0.5 eV near $\overline{K}$ and 0.7 eV at $\overline{M}$, and touches E_F at midpoints between $\overline{M}$ and $\overline{K}$. The U_5 band dispersing downward from $\overline{M}$ at E_F shows a minimum at between the $\overline{M}$ and $\overline{K}$ points, and extends in the energy range of 0.6–0.9 eV toward $\overline{\Gamma}$. The complicated structures of the U_4 and U_5 bands along $\overline{K}$-$\overline{M}$-$\overline{K}$ correspond to the region where the Fermi contours deviate from the circles.

In order to gain insight into the origin of the two inner and outer Fermi circles, we calculated the electronic band structure. Figure 8(a) shows the calculated band structure of the triple-layer (In, Mg)/Si(111) ($\sqrt{3}\times\sqrt{3}$) model in Fig. 3. The sizes of circles and squares are proportional to the contribution of In $5sp$ and Mg $3s$, respectively. The color scale of the circles represents the relative contribution of In $5sp_xp_y$ and $5p_z$, where the z axis is normal to the surface. There is good agreement between the theoretical and experimental band structure. The experimentally identified U_1–U_6 bands are reproduced except that the downward dispersion toward $\overline{M}$ of the U_4 band lies at lower binding energy than that in the experiment. Some of the calculated bands are hardly detectable in the experimental band structure due to matrix element effects. For example, the U_1, U_2, and U_3 bands highlighted by the thick yellow (light gray) curves along $\overline{\Gamma}$-$\overline{M}$ are clearly detected in the ARPES band map of Fig. 6(b), but the bands between U_2 and U_3, and outside U_3 with smaller slopes are only faintly seen.

Note that the band marked by the red arrows in Figs. 6(a) and 6(c) is observed between the U_4 and U_6 bands and crosses E_F at 1.38 Å^{-1} along $\overline{\Gamma}$-$\overline{K}$. This band does not appear in the calculated band structure in Fig. 8(a). The k_F value is smaller than that of the double-layer $2\sqrt{3}$ phase (1.42 Å^{-1}), and only the ($\sqrt{3}\times\sqrt{3}$) pattern is observed in LEED [Fig. 1(e)]. We ascribe the band to a double-layer ($\sqrt{3}\times\sqrt{3}$) phase. We found that the most stable double-layer ($\sqrt{3}\times\sqrt{3}$) model is the In$_5$Mg$_3$ structure with stacking of the top In$_4$ and bottom
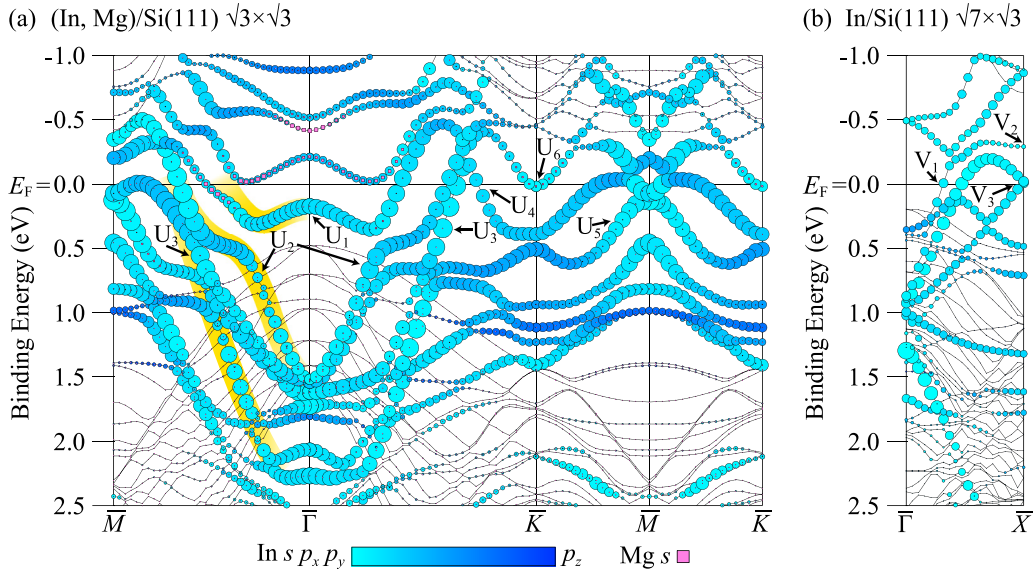
FIG. 8. Calculated band structure of (a) the triple-layer (In, Mg)/Si(111) ($\sqrt{3}\times\sqrt{3}$) phase and (b) the double-layer In/Si(111) ($\sqrt{7}\times\sqrt{3}$) phase. The sizes of the circles and squares are proportional to the contribution of In $5sp$ and Mg $3s$, respectively. The relative contribution of In $5sp_xp_y$ and $5p_z$ is shown by color scale. The thick yellow (light gray) curves highlight the U_1–U_3 bands clearly detected in the ARPES band map along $\overline{\Gamma}$-$\overline{M}$ [Fig. 6(b)].

In_1Mg_3 layers of the model in Fig. 3. The structure is quite similar to the double-layer structure of the (Tl, Mg)/Si(111) ($\sqrt{3}\times\sqrt{3}$) phase and exhibits similar band structure with that calculated for the (Tl, Mg)/Si(111) phase without spin-orbit coupling [37]. It has a metallic band located between the U_4 and U_6 bands of the triple-layer phase, which coincides with the experimentally observed one. The double-layer $\sqrt{3}$ phase is much less stable by > 250 meV per unit cell than the triple-layer $\sqrt{3}$ phase, but it should coexist as a minor phase to compensate the loss of the In coverage. In the STM experiments, the double-layer $\sqrt{3}$ phase is observed as a minor domain surrounded by the triple-layer phase with domain size of 400–600 Å, which results in the weak but sharp band observed in ARPES. The double-layer $\sqrt{3}$ phase must be more stable than the double-layer $2\sqrt{3}$ phase, given the stable configuration of the bottom In_1Mg_3 layer of the $\sqrt{3}$ phase. The double-layer $2\sqrt{3}$ phase is stable under the condition of small Mg coverage up to 0.25 ML, and with increasing coverage the triple-layer $\sqrt{3}$ phase as well as minor double-layer $\sqrt{3}$ phase grow.

The surface-state bands of the triple-layer $\sqrt{3}$ phase are predominantly composed of In $5s$ and $5p$ orbitals. A small contribution of the Mg $3s$ orbital is found mainly in the unoccupied bands near $\overline{\Gamma}$, indicating that the Mg atoms are almost completely ionized. Highly dispersive bands including the U_1, U_2 and U_3 bands have In $5sp_xp_y$ character. On the other hand, flat bands, for instance at ~ 1.0 eV below E_F along $\overline{K}$-$\overline{M}$-$\overline{K}$, have In $5p_z$ character. The flat bands at 0–1.0 eV above E_F have a large contribution from the $5p_z$ orbital of the top In_1 atom of Fig. 3(c), while those of the other top In atoms primarily contribute to the bands below E_F. This explains the simulated STM images in Fig. 3(d) with the In_1 atom brightly visible only at the positive sample bias.

Figure 9(a) shows the charge density distributions of the U_3 and U_1 states at E_F along $\overline{\Gamma}$-$\overline{K}$. As expected from their In $5sp_xp_y$ character, both the U_3 and U_1 states have wave functions widely distributed in the in-plane direction. However, they show striking difference along the out-of-plane ([111]) direction. The U_3 state is spread over the three metal layers with a broad peak centered at the middle layer in the in-plane averaged charge density plot [the right panel of Fig. 9(a)]. On the other hand, the U_1 state has two peaks: one is localized in the top layer, and the other is located in the middle and bottom layers. The two different vertical charge distributions indicate states with zero and one nodal planes parallel to the surface, or in other words, bonding and antibonding states between the top In layer and the middle-bottom (In, Mg) layers. The bonding character is also found in the U_2 and U_4 bands along $\overline{\Gamma}$-$\overline{K}$, which correspond to the outer Fermi circle [orange (light gray) curves in Fig. 7(a)], and the antibonding character is in the U_6 band at $\overline{K}$, which corresponds to the inner Fermi circle [black curves in Fig. 7(a)]. We therefore conclude that the two Fermi circles are due to the bonding and antibonding states between the top and middle-bottom layers. The outer circle comes from the bonding states with higher binding energy, and the inner circle from the antibonding states with lower binding energy.

Let us now compare the electronic states of the triple-layer (In, Mg)/Si(111) ($\sqrt{3}\times\sqrt{3}$) phase with those of the double-layer In/Si(111) ($\sqrt{7}\times\sqrt{3}$) phase. The In/Si(111) ($\sqrt{7}\times\sqrt{3}$) phase has 2D nearly free-electron band structure [12,16–18,36]. Most of the Fermi surface is parts of a circle folded into the ($\sqrt{7}\times\sqrt{3}$) SBZ except for butterfly features as indicated in Fig. 7(b). The arcs extending along $\overline{\Gamma}$-$\overline{Y}$ is ascribed to the V_1 band in the calculated band structure along $\overline{\Gamma}$-$\overline{X}$ in Fig. 8(b). The V_1 band is of In $5sp_xp_y$ character. The charge distribution shown in Fig. 9(b) clearly indicates that

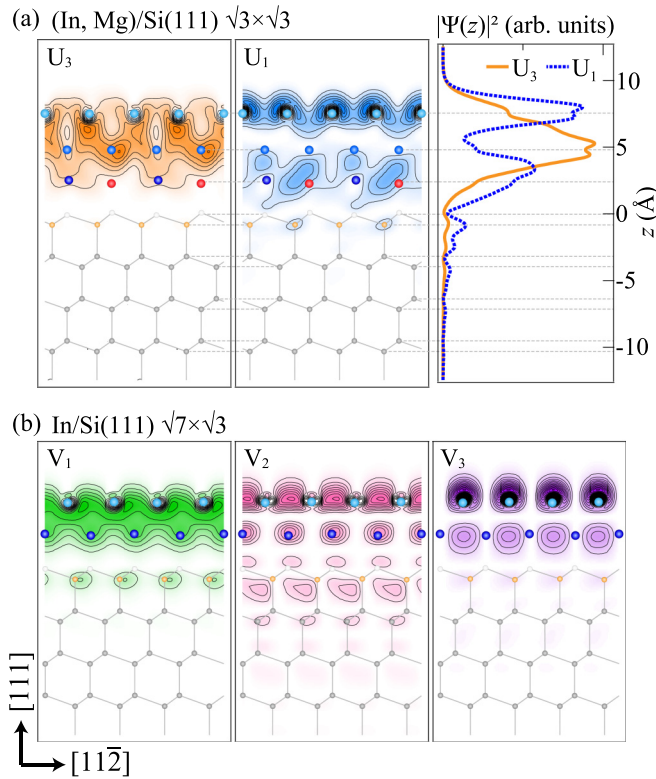(a) (In, Mg)/Si(111) √3×√3

(b) In/Si(111) √7×√3

FIG. 9. (a) Charge density distributions in the $(1\bar{1}0)$ plane [the thick dotted line in Fig. 3(c)] of the (left) U_3 state and (middle) U_1 state at E_F along $\overline{\Gamma}$-$\overline{K}$ of the triple-layer (In, Mg)/Si(111) ($\sqrt{3}\times\sqrt{3}$) phase. The right panel of (a) displays the in-plane averaged charge density distributions along z, the [111] direction, of the U_3 and U_1 states. (b) Charge density distributions in the $(1\bar{1}0)$ plane of the (left) V_1, (middle) V_2, and (right) V_3 states along $\overline{\Gamma}$-$\overline{X}$ of the double-layer In/Si(111) ($\sqrt{7}\times\sqrt{3}$) phase. The atom positions are indicated by circles whose colors are the same as in Fig. 3.

the V_1 band is a bonding state between the top and bottom In layers. Most of the metallic bands of the ($\sqrt{7}\times\sqrt{3}$) phase show bonding character, which was also reported in the previous calculation (see H–N states of Fig. 6 of Ref. [18]). This shows that the circular Fermi surface is attributed to the bonding states. The antibonding states between the In layers have little contribution to metallic bands because of mixing with Si dangling-bond states. For example, the V_2 state has antibonding character with a nodal plane between the two In layers. It also has large Si contribution with antibonding character with respect to In-Si bonds, and thus it is located above E_F. An exception is seen in the butterfly parts of the Fermi surface. The V_3 band forming the butterfly wing near $\overline{X}$ shows antibonding character. However, it does not mix with Si dangling-bond states and remain metallic. This is because the V_3 state has nodal planes perpendicular to surface, and the positions of the top Si atoms coincide with one of the nodal planes. In the double-layer $2\sqrt{3}$ phase with an almost perfect single Fermi circle [Fig. 5(a)], we consider that only the bonding states contribute to the metallic bands and that the antibonding states completely disappear due to lack of a special symmetrical relationship as in the case of the In/Si(111) ($\sqrt{7}\times\sqrt{3}$) phase.

In the triple-layer $\sqrt{3}$ phase, the charge density difference in Fig. 4 shows that the In_1Mg_3 bottom layer plays a major role in bonding with Si and that the top and middle layers remain almost intact. The metallic bands of the $\sqrt{3}$ phase is mainly composed of In orbitals and many of the In atoms are located in the top and middle layers, and hence, the metallic bands are almost unaffected by the Si dangling-bond states. This realizes the two concentric Fermi circles with bonding and antibonding character, which are characteristic of freestanding double-layer In films. Note that the charge distributions of the U_3 and U_1 states [Fig. 9(a)] extend to the bottom layer. It is more accurate to say that the two Fermi circles come from the bonding and antibonding states between the top and middle-bottom layers, and that the middle-bottom layer contributes both to the metallic bands and the termination of the Si dangling bonds.

The bonding and antibonding states with zero and one nodal planes in the $\sqrt{3}$ phase are different from well-known quantum well states with one and two antinodes in thin metal films with thickness typically larger than five layers. The antinodes of the quantum well states arise from envelope functions due to the out-of-plane confinement of oscillating bulk Bloch waves [46,47]. Instead, the electronic properties of the $\sqrt{3}$ phase can be regarded as atomically ultrathin quantum well states, which have been less explored because of the diffculty in creating well-ordered metal films with a-few-layer thickness [48–51]. Contrary to the previous studies examining various surface structures as buffer layers, we propose a new method to create a buffer layer by Mg deposition onto ultrathin metal films on Si(111). In this work, we established the triple-atomic-layer metal films exhibiting electronic properties of nearly freestanding double layers with a buffer layer. Double-layer films with a single layer on the buffer layer could be obtained by using a single-layer phase of In/Si(111) [4,27] instead of the double-layer In/Si(111) as pristine structure. Films of thickness more than two layers may also be formed by In deposition onto the triple-layer films, considering the little difference in in-plane atom density between the films on Si(111) and bulk In. This demonstrates the possibility of (In, Mg)/Si(111) becoming a beneficial model for exploring evolution of metallic electronic properties from 2D to 3D.

IV. SUMMARY

We have studied the structural and electronic properties of two new metallic phases obtained by Mg deposition onto the double-layer In/Si(111) ($\sqrt{7}\times\sqrt{3}$) phase. The ($2\sqrt{3}\times2\sqrt{3}$) phase is considered to have double-layer structure. It shows 2D free-electron-like electronic structure with a circular Fermi surface, similar to that of the In/Si(111) ($\sqrt{7}\times\sqrt{3}$) phase. The ($\sqrt{3}\times\sqrt{3}$) phase consists of three hexagonal close-packed metal layers stacked in an ABC sequence. The ($\sqrt{3}\times\sqrt{3}$) phase also has free-electron-like electronic structure, but the Fermi surface is composed of two circles with different radii. The two Fermi circles are associated with bonding and antibonding states with zero and one nodal planes between the top and middle layers. The bottom layer consisting of three Mg atoms and an In atom per ($\sqrt{3}\times\sqrt{3}$) unit cell serves as a buffer layer to decouple the metallic bands from Si dangling-bond states and realize a nearly freestanding double-layer metal.

[1] M. Hupalo, T. L. Chan, C. Z. Wang, K. M. Ho, and M. C. Tringides, Phys. Rev. B **66**, 161410(R) (2002).

[2] S. Stepanovsky, M. Yakes, V. Yeh, M. Hupalo, and M. C. Tringides, Surf. Sci. **600**, 1417 (2006).

[3] T. Kuzumaki, T. Shirasawa, S. Mizuno, N. Ueno, H. Tochihara, and K. Sakamoto, Surf. Sci. **604**, 1044 (2010).

[4] S. Terakawa, S. Hatta, H. Okuyama, and T. Aruga, Phys. Rev. B **100**, 115428 (2019).

[5] T. Shirasawa, S. Yoshizawa, T. Takahashi, and T. Uchihashi, Phys. Rev. B **99**, 100502(R) (2019).

[6] S. S. Lee, H. J. Song, N. D. Kim, J. W. Chung, K. Kong, D. Ahn, H. Yi, B. D. Yu, and H. Tochihara, Phys. Rev. B **66**, 233312 (2002).

[7] A. N. Mihalyuk, L. V. Bondarenko, A. Y. Tupchaya, D. V. Gruznev, J. P. Chou, C. R. Hsing, C. M. Wei, A. V. Zotov, and A. A. Saranin, Surf. Sci. **668**, 17 (2018).

[8] A. A. Baski, S. C. Erwin, M. S. Turner, K. M. Jones, J. W. Dickinson, and J. A. Carlisle, Surf. Sci. **476**, 22 (2001).

[9] M. H. Kang, J. H. Kang, and S. Jeong, Phys. Rev. B **58**, R13359 (1998).

[10] D. Lee, G. Lee, S. Kim, C. Hwang, J. Y. Koo, and H. Lee, J. Phys.: Condens. Matter **19**, 266004 (2007).

[11] K. Kataoka, K. Hattori, Y. Miyatake, and H. Daimon, Phys. Rev. B **74**, 155406 (2006).

[12] E. Rotenberg, H. Koh, K. Rossnagel, H. W. Yeom, J. Schäfer, B. Krenzer, M. P. Rocha, and S. D. Kevan, Phys. Rev. Lett. **91**, 246404 (2003).

[13] T. Zhang, P. Cheng, W.-J. Li, Y.-J. Sun, G. Wang, X.-G. Zhu, K. He, L. Wang, X. Ma, X. Chen, Y. Wang, Y. Liu, H.-Q. Lin, J.-F. Jia, and Q.-K. Xue, Nat. Phys. **6**, 104 (2010).

[14] T. Uchihashi, P. Mishra, M. Aono, and T. Nakayama, Phys. Rev. Lett. **107**, 207001 (2011).

[15] M. Yamada, T. Hirahara, and S. Hasegawa, Phys. Rev. Lett. **110**, 237001 (2013).

[16] S. Yoshizawa, T. Kobayashi, Y. Nakata, K. Yaji, K. Yokota, F. Komori, S. Shin, K. Sakamoto, and T. Uchihashi, Nat. Commun. **12**, 1462 (2021).

[17] J. W. Park and M. H. Kang, Phys. Rev. Lett. **109**, 166102 (2012).

[18] K. Uchida and A. Oshiyama, Phys. Rev. B **87**, 165433 (2013).

[19] S. L. Surnev, J. Kraft, and F. P. Netzer, J. Vac. Sci. Technol. A **13**, 1389 (1995)

[20] F. P. Leisenberger, H. Öfner, M. G. Ramsey, and F. P. Netzer, Surf. Sci. **383**, 25 (1997).

[21] I. B. Altfeder, X. Liang, T. Yamada, D. M. Chen, and V. Narayanamurti, Phys. Rev. Lett. **92**, 226404 (2004).

[22] J. Chen, M. Hupalo, M. Ji, C. Z. Wang, K. M. Ho, and M. C. Tringides, Phys. Rev. B **77**, 233302 (2008).

[23] J. H. Dil, B. Hülsen, T. U. Kampen, P. Kratzer, and K. Horn, J. Phys.: Condens. Matter **22**, 135008 (2010).

[24] Y. Liu, T. Miller, and T. C. Chiang, J. Phys.: Condens. Matter **23**, 365302 (2011).

[25] A. Gray, Y. Liu, H. Hong, and T.-C. Chiang, Phys. Rev. B **87**, 195415 (2013).

[26] J. W. Park and M. H. Kang, Phys. Rev. Lett. **117**, 116102 (2016).

[27] S. Terakawa, S. Hatta, H. Okuyama, and T. Aruga, J. Phys.: Condens. Matter **30**, 365002 (2018).

[28] K. S. An, R. J. Park, J. S. Kim, C. Y. Park, S. B. Lee, T. Abukawa, S. Kono, T. Kinoshita, A. Kakizaki, and T. Ishii, J. Appl. Phys. **78**, 1151 (1995).

[29] O. Bunk, G. Falkenberg, J. H. Zeysing, L. Lottermoser, R. L. Johnson, M. Nielsen, F. Berg-Rasmussen, J. Baker, and R. Feidenhans'l, Phys. Rev. B **59**, 12228 (1999).

[30] P. E. Blöchl, Phys. Rev. B **50**, 17953 (1994).

[31] G. Kresse and D. Joubert, Phys. Rev. B **59**, 1758 (1999).

[32] G. Kresse and J. Hafner, Phys. Rev. B **47**, 558 (1993).

[33] G. Kresse and J. Furthmüller, Phys. Rev. B **54**, 11169 (1996).

[34] J. P. Perdew, K. Burke, and M. Ernzerhof, Phys. Rev. Lett. **77**, 3865 (1996).

[35] H. J. Monkhorst and J. D. Pack, Phys. Rev. B **13**, 5188 (1976).

[36] T. Kobayashi, Y. Nakata, K. Yaji, T. Shishidou, D. Agterberg, S. Yoshizawa, F. Komori, S. Shin, M. Weinert, T. Uchihashi, and K. Sakamoto, Phys. Rev. Lett. **125**, 176401 (2020).

[37] A. Y. Tupchaya, L. V. Bondarenko, Y. E. Vekovshinin, A. A. Yakovlev, A. N. Mihalyuk, D. V. Gruznev, C. R. Hsing, C. M. Wei, A. V. Zotov, and A. A. Saranin, Phys. Rev. B **101**, 235444 (2020).

[38] A. A. Nayeb-Hashemi and J. B. Clark, Bull. Alloy Phase Diag. **6**, 149 (1985).

[39] P. Villars and K. Girgis, Z. Metallkd. **73**, 169 (1982).

[40] J. Tersoff and D. R. Hamann, Phys. Rev. B **31**, 805 (1985).

[41] S. N. Takeda, N. Higashi, and H. Daimon, Phys. Rev. Lett. **94**, 037401 (2005).

[42] H. Lüth, *Solid Surfaces, Interfaces and Thin Films* (Springer, Berlin, Heidelberg, 2010).

[43] D. C. Gleason-Rohrer, B. S. Brunschwig, and N. S. Lewis, J. Phys. Chem. C **117**, 18031 (2013).

[44] M. D'angelo, M. Konishi, I. Matsuda, C. Liu, S. Hasegawa, T. Okuda, and T. Kinoshita, Surf. Sci. **590**, 162 (2005).

[45] G. R. Castro, P. Pervan, E. G. Michel, R. Miranda, and K. Wandelt, Vacuum **41**, 564 (1990).

[46] T. C. Chiang, Surf. Sci. Rep. **39**, 181 (2000).

[47] V. N. Strocov, J. Electron Spectrosc. Relat. Phenom. **229**, 100 (2018).

[48] Z. Tang, J. Teng, Y. Jiang, J. Jia, J. Guo, and K. Wu, J. Appl. Phys. **102**, 053504 (2007).

[49] S. Starfelt, L. S. Johansson, and H. M. Zhang, Surf. Sci. **682**, 25 (2019).

[50] S. Starfelt, R. Lavén, L. S. Johansson, and H. M. Zhang, Surf. Sci. **701**, 121697 (2020).

[51] M. Hell, N. Ehlen, G. Marini, Y. Falke, B. V. Senkovskiy, C. Herbig, C. Teichert, W. Jolie, T. Michely, J. Avila, G. D. Santo, D. M. la Torre, L. Petaccia, G. Profeta, and A. Grüneis, Nat. Commun. **11**, 1340 (2020).